


## Origin of the isostructural electronic states of the topological insulator $\text{Bi}_2\text{Te}_3$

Xinguo Hong <sup>1,\*</sup>, Matt Newville,<sup>2</sup> Yang Ding,<sup>1</sup> Dongzhou Zhang,<sup>2</sup> Tetsuo Irifune,<sup>3</sup> Genda Gu,<sup>4</sup> and Ho-Kwang Mao<sup>1,5</sup>

<sup>1</sup>Center for High Pressure Science and Technology Advanced Research, Beijing 100094, People's Republic of China

<sup>2</sup>Consortium for Advanced Radiation Sources, University of Chicago, Chicago, Illinois 60637, USA

<sup>3</sup>Geodynamics Research Center, Ehime University, Matsuyama 790–8577, Japan

<sup>4</sup>Condensed Matter Physics and Materials Science Department, Brookhaven National Laboratory, Upton, New York 11973, USA

<sup>5</sup>Geophysical Laboratory, Carnegie Institution of Washington, Washington, DC 20015, USA



(Received 5 July 2020; accepted 24 September 2020; published 16 October 2020)

The novel physics, such as the pressure-induced electronic topological transition (ETT), topological superconductivity and Majorana fermions in the isostructural  $R\text{-}3m$  phase of three-dimensional topological insulator  $\text{Bi}_2\text{Te}_3$ , holds considerable interest in condensed-matter physics. We carried out a combined investigation of single-crystal x-ray diffraction, high-quality x-ray absorption fine structure, and first-principles theoretical calculations to decipher the puzzling origin of the intriguing electronic states in the isostructural  $R\text{-}3m$  phase of  $\text{Bi}_2\text{Te}_3$  at high pressure. Three distinct regions with two isostructural phase transitions (IPTs) in the  $R\text{-}3m$  phase have been identified. The first IPT, which is known as the ETT, occurs at the boundary of region I (0–2 GPa) and region II (2–5 GPa) with a sharp minimum in the  $c/a$  ratio of  $R\text{-}3m$  structure, while the second IPT happens as pressure increases from region II (2–5 GPa) to region III (5–7 GPa). The positions of the Bi (6c) and Se (6c) sites in the unit cell change rapidly in region II (2–5 GPa), but there is little change at these sites in region III (5–7 GPa). The band-gap closure in region I reflects the pressure-induced metallization. At higher pressures, the band gap opens in region II but remains almost constant after the second IPT in region III, which agrees well with the topological superconductivity of  $\text{Bi}_2\text{Te}_3$ . Our results demonstrate that the combination of local structure, long-range crystal structure, and first-principles calculation is critically important for understanding the isostructural electronic states and the connection between the structure and function as in  $\text{Bi}_2\text{Te}_3$  at high pressure.

DOI: [10.1103/PhysRevB.102.134110](https://doi.org/10.1103/PhysRevB.102.134110)

### I. INTRODUCTION

The electronic state of three-dimensional (3D) topological insulator (TI)  $\text{Bi}_2\text{Te}_3$  at ambient conditions has been extensively studied [1–5]. Applying pressure can tune the topological electronic states and physical properties without introducing chemical doping disorder [6]. Under high pressure, the layered 3D TIs ( $\text{Bi}_2\text{Se}_3$ ,  $\text{Bi}_2\text{Te}_3$ , and  $\text{Sb}_2\text{Te}_3$ ) show a common pressure-induced electronic topological transition (ETT) or isostructural phase transition (IPT) at 2–4 GPa [7], and topological superconductivities [8–10]. However, the rhombohedral  $R\text{-}3m$  isostructural phase of  $\text{Bi}_2\text{Te}_3$  (space group No. 166) remains a puzzling mystery. Within the same  $R\text{-}3m$  phase, the ETT leads to considerable changes and anomalies in the mechanical, vibrational, electrical, thermodynamic, and transports properties [11,12]. The pressure-induced topological superconductivity in the  $R\text{-}3m$  phase is fundamentally important because of the long-sought Majorana fermions, which have potential applications in quantum computing [5]. The underlying mechanism of ETT [13,14], structural origin of metallization [10,15] and topological superconductivity [6,16], and the interplay between the bulk and surface states [17] remain elusive.

Understanding the novel physics in the  $R\text{-}3m$  phase critically depends on knowledge of the crystal structure, electronic band structure, bulk and surface electronic states, carrier concentration, and spin-orbit interactions [2]. Therefore, the local structure of the  $R\text{-}3m$  phase is of great interest. So far, x-ray diffraction (XRD) has played a dominant role in structure determination at high pressure [18], while high-quality x-ray absorption fine-structure (XAFS) measurement using nanopolycrystalline diamond (NPD) anvils for local structure under pressure in the 3D TIs is very rare [19]. XAFS measurements on  $\text{Bi}_2\text{Te}_3$  with conventional single-crystal diamond anvils have been reported previously [20,21]. However, it remains unclear how the local structure of  $\text{Bi}_2\text{Te}_3$  changes during the ETT because of considerable uncertainties either in the pressure range of ETT ( $\sim 5$  GPa) itself or in the values of Bi-Te/Bi bond lengths possibly due to the limited spectral range ( $< 11 \text{ \AA}^{-1}$ ) [20,21]. Conventional powder XRD is a powerful tool to characterize the structural phase transition at high pressure, but it is difficult to determine the local structure and the precise Wyckoff positions of atoms in the crystal. Consequently, the XRD proof for ETT remains divergent [7,14,22–24]. X-ray absorption fine structure spectroscopy is a well-established technique to probe the local atomic and electronic structure around the absorber atoms in materials. However, high-pressure XAFS suffers from Bragg reflections of single-crystal diamond anvils [25]. Recently,

\*xinguo.hong@hpstar.ac.cn

NPD anvils, which consist of randomly oriented nanograined diamonds, have proven promising for glitch-free XAFS spectra [26]. In this paper, we report a combined investigation of single-crystal x-ray diffraction (SC-XRD), high-pressure (HP)-XAFS using NPD anvils, and first-principles calculations for  $\text{Bi}_2\text{Te}_3$  up to 14 GPa.

## II. EXPERIMENTAL

### A. Crystal growth and preparation

The  $\text{Bi}_2\text{Te}_3$  single crystals in this work were grown by a unidirectional solidification method with slowly cooling down. The sample was cleaved along the  $c$  axis from a bulk  $\text{Bi}_2\text{Te}_3$  single crystal and cut into suitable small chips loaded into the sample chamber of Re gasket. Conventional diamond-anvil cell (DAC) was employed for single-crystal XRD experiments, while NPD cells were used for high-pressure XAFS measurements. Neon gas was loaded in the DACs as a pressure-transmitting medium. Ruby chips were placed at the edge of the sample chamber for pressure determination using the ruby fluorescence technique [27]. The quasi-hydrostatic conditions were maintained throughout the experiments by monitoring the separation and widths of both  $R1$  and  $R2$  lines.

### B. High-pressure synchrotron single-crystal x-ray diffraction

A membrane-pressurization system was used in the single-crystal (SC)-XRD experiment in order to collect diffraction data at small pressure steps, which is necessary to probe the subtle changes in the lattice parameters of  $\text{Bi}_2\text{Te}_3$  crystals at high pressure. At each pressure point, a set of angular dispersive XRD of  $\text{Bi}_2\text{Te}_3$  single crystal was collected using Pilatus 1M detector over the  $33^\circ$  DAC opening with  $1^\circ$  step at the 13-BM-C beamline, Advanced Photon Source (APS), Argonne National Laboratory. This Pilatus detector facilities fast data collection of 33 diffraction images at each pressure point, which were then combined into a single diffraction file. The x-ray energy was fixed at 28.568 keV. The size of focused x-ray beam was  $12 \mu\text{m}$  (V)  $\times$   $18 \mu\text{m}$  (H). The sample-detector distance and detector orientation were calibrated using a  $\text{LaB}_6$  standard. Pressure was measured both before and after every XAFS or XRD measurement and the pressure difference was typically 0.3 GPa or less. The two-dimensional image plate patterns were integrated to the one-dimension patterns by using the FIT2D software [28]. The resulting diffraction patterns were fitted via Le Bail and Rietveld refinements of  $R-3m$  structure using JANA2006 [29] and GSAS [30] packages.

### C. High-pressure XAFS

A Princeton-manufactured large-opening symmetrical diamond-anvil cell (DAC) was employed with a pair of  $600 \mu\text{m}$  culet NPD anvils. A rectangle foil of rhenium was pre-indented down to a thickness of  $40 \mu\text{m}$ . A gasket hole of  $220 \mu\text{m}$  was drilled at the indentation center in the Re foil. XAFS experiments were carried out at Bi  $L_3$ -edge of  $\text{Bi}_2\text{Te}_3$  powder sample in the transmission mode at the GeoSoilEnviroCARS undulator beamline 13-ID-E, APS, Argonne National Laboratory. The x-ray beam size was focused

down to a square spot of  $1\text{--}2 \mu\text{m}$  size using Kirkpatrick-Baez mirrors that were spatially stable over the entire energy scan. XAFS spectra were collected with 5-eV steps before the main edge, 0.2-eV steps from  $-10$  to  $25$  eV across the Bi  $L_3$ -edge ( $13\,419$  eV), and  $0.05\text{-}\text{\AA}^{-1}$  steps in  $k$  space to  $14 \text{\AA}^{-1}$  above the main edge.

At each pressure point, multiple data were collected at different angle settings with respect to the incident x-ray beam, e.g., typically from  $-3^\circ$  to  $+3^\circ$  with  $0.5$  or  $1^\circ$  interval [25], in order to minimize the residual grain-size effect of the NPD anvils, as well as to increase the XAFS statistics. Different sample spots were also surveyed so as to mitigate/check the x-ray induced radiation damage. XAFS data analysis were performed using the ATHENA and ARTEMIS programs [31] implemented in the IFEFFIT package [32].

### D. Density-functional calculation

Density-functional theory calculations were performed using the Perdew-Zunger-type [33] generalized gradient approximation [34] implemented in the QUANTUMESPRESSO code [35]. Full relativistic pseudopotentials ( $\text{Bi.rel-pz-dn-rrkjus\_psl.1.0.0.UPF}$  and  $\text{Te.rel-pz-dn-rrkjus\_psl.0.2.2.UPF}$ ) were used in the calculation of the bulk electronic structure of  $\text{Bi}_2\text{Te}_3$ . Spin-orbit coupling (SOC) has been included. The calculations were performed with a plane-wave cutoff of 50 Ry on an  $8 \times 8 \times 8$   $k$ -point mesh. The lattice parameters were determined by SC-XRD experiment, but the Wyckoff positions of atoms were calculated from the Bi-Te bond length obtained by HP-XAFS experiment. At each pressure step, we calculated band structures along the high-symmetry lines ( $\Gamma$ - $Z$ - $F$ - $\Gamma$ - $L$ ) in the Brillouin zone of  $R-3m$  structure. The values of band gap were computed with and without XAFS optimization on the Wyckoff positions of atoms for comparison.

## III. RESULTS AND DISCUSSION

$\text{Bi}_2\text{Te}_3$  has a layered tetradymite crystal structure with space group ( $R-3m$ , No. 166) [36]. At ambient pressure,  $\text{Bi}_2\text{Te}_3$  crystal contains five atomic planes with Te2-Bi-Te1-Bi-Te2 stacking in a quintuple layer (QL) along the  $c$  axis. The Bi sites locate inside the QL, while there are two inequivalent Te atoms (Te1 and Te2) occupying the central and the outermost planes of a QL, respectively. The Te1 site in the central plane of QL is the inversion center of the  $R-3m$  structure. Bonds inside the quintuple layer are of ionic-covalent type, while the outermost Te2-Te2 bonds between adjacent QLs are linked by weak van der Waals forces. There are two types of Bi-Bi bonds, namely short bonds in the Bi plane and other longer bonds between the Bi plane.

We designed two complementary experiments to address the structural variation of  $\text{Bi}_2\text{Te}_3$  at high pressure. The Bi  $L_3$ -edge XAFS experiment aimed to measure the ionic-covalent Bi-Te and Bi-Bi bonds inside the QLs ( $r_{\text{Bi-Te1}}$ ,  $r_{\text{Bi-Te2}}$ , and  $r_{\text{Bi-Bi}}$ ). SC-XRD was employed to measure the lattice parameters of  $\text{Bi}_2\text{Te}_3$  and monitor the phase transition at high pressure.

Figure 1 shows the selected angle-dispersive XRD patterns of  $\text{Bi}_2\text{Te}_3$  crystal at various pressures from 1.0

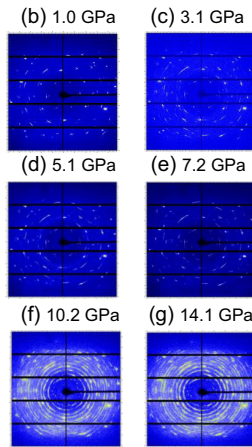
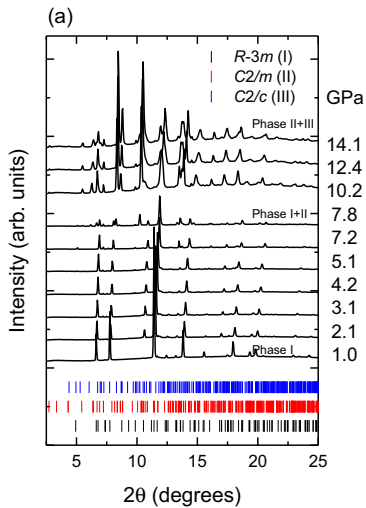


FIG. 1. (a) The selected angle-dispersive single-crystal XRD patterns of  $\text{Bi}_2\text{Te}_3$  under various pressures at room temperature from 1.0 to 14.1 GPa. The vertical bars are the expected diffraction lines of  $R-3m$  ( $\alpha\text{-Bi}_2\text{Te}_3$ ),  $C2/m$  ( $\beta\text{-Bi}_2\text{Te}_3$ ), and  $C2/c$  ( $\gamma\text{-Bi}_2\text{Te}_3$ ) phases at 1.0, 12, and 14 GPa, respectively. (b)–(f) The combined 2D XRD images at various pressures, which were collected with  $1^\circ$  step over the  $33^\circ$  cell open at the 13-BM-C beamline, APS.

to 14.1 GPa. It is recognized that crystal structure holds the key to understand the intriguing novel physics of  $\text{Bi}_2\text{Te}_3$  at high pressure, so the structural phase transitions of  $\text{Bi}_2\text{Te}_3$  have been studied repeatedly [21,22,24,37,38]. It is clear that  $\text{Bi}_2\text{Te}_3$  undergoes a phase transition sequence of  $R-3m$  ( $\alpha\text{-Bi}_2\text{Te}_3$ )  $\rightarrow$   $C2/m$  ( $\beta\text{-Bi}_2\text{Te}_3$ )  $\rightarrow$   $C2/c$  ( $\gamma\text{-Bi}_2\text{Te}_3$ )  $\rightarrow$   $Im-3m$  ( $\delta\text{-Bi}_2\text{Te}_3$ ) structures at high pressure with relatively broad phase boundaries [21,37,38]. The reported phase transition of  $R-3m \rightarrow C2/m$  in  $\text{Bi}_2\text{Te}_3$  occurs at pressures above 8 GPa [21,22,24,37,38]. As shown in Fig. 1, there is little change in the two-dimensional (2D) x-ray diffraction images from 1.0 to 7.2 GPa [Figs. 1(b)–1(e)], indicating the near integrity of  $\text{Bi}_2\text{Te}_3$  single crystal in the  $R-3m$  phase in DAC up to 7.2 GPa without emergence of appreciable amount of  $C2/m$  phase [Fig. 1(a)]. The diffraction pattern is mixed with the diffraction peaks of  $C2/m$  phase ( $\beta\text{-Bi}_2\text{Te}_3$ ) at 7.8 GPa, being consistent with previous observations [21,22,24,37,38]. As pressure increases to 10.2 GPa, the crystal of  $R-3m$  phase is totally destroyed and broken down into small pieces with diffraction ring features close to a typical powder x-ray diffraction measurement [Figs. 1(f) and 1(g)].

SC-XRD under high pressure allows one to determine the lattice parameters with high accuracy, but is especially challenging owing to the limited access to reciprocal space afforded by the high-pressure apparatus and the diffraction system for accurate diffraction intensity and  $d$ -spacing measurement [39]. Unlike the case of powder x-ray diffraction, special care is required to avoid any destruction of the single crystal, which is hard to control in high-pressure experiment, because destruction or even change in the preferred orientation of single crystal in DAC can significantly alter the Bragg peak intensities of x-ray diffraction. The lattice parameters are relatively easy to measure with high accuracy, but structural

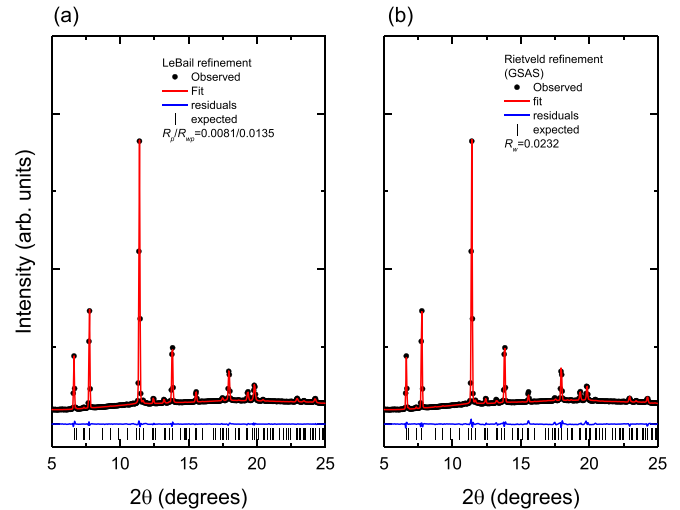


FIG. 2. (a) The representative LeBail refinement using JANA2006 software [29] and (b) Rietveld refinement using GSAS [30] with spherical harmonics in the preferred orientation model for the single-crystal x-ray data of  $\text{Bi}_2\text{Te}_3$   $R-3m$  phase at 1 GPa.

parameters (atomic positions) depend on the accurate intensities of x-ray diffraction. There are two ways to determine the structural parameters at high pressure. One is through Rietveld refinement merely, and the other is the combined method of HP-XAFS and LeBail/Rietveld refinement, as reported in the recent  $\text{Bi}_2\text{Se}_3$  experiments [19].

Figure 2 shows the representative LeBail refinement [Fig. 2(a)] and Rietveld refinement [Fig. 2(b)] for the single-crystal x-ray data of  $R-3m$  phase in  $\text{Bi}_2\text{Te}_3$  at 1 GPa using JANA2006 [29] and GSAS [30] software, respectively. Refinement with LeBail technique is a good choice for the precise determination of lattice parameters of  $R-3m$  phase, because this structureless technique does not require a set of Bragg peaks with accurate diffraction intensities. After LeBail refinement is completed, we do not optimize the atomic position because XAFS is much more sensitive for subtle change in bond length or the relative atomic distance than x-ray diffraction. It is known that x-ray-diffraction intensity depends on the crystal orientations, grain size, and texture, etc., which are difficult to control under high pressure. However, it is well recognized that without the help of XAFS, the atom position can be optimized by Rietveld refinement based on the diffraction data. Figure 2(b) shows a decent Rietveld refinement using GSAS [30] with spherical harmonics in the preferred orientation model for the SC-XRD data of  $\text{Bi}_2\text{Te}_3$ . Additional Rietveld refinement was also conducted using JANA2006 [29] with (1 1 0) preferred orientation of the  $\text{Bi}_2\text{Te}_3$  single crystal in DAC. This (1 1 0) preferred orientation basically retains up to 7.2 GPa [Figs. 1(b)–1(e)]. Although the residual of Rietveld refinement is slightly larger than that of LeBail refinement, it is worthwhile to complete Rietveld refinement because it can verify the value of structural parameters obtained by XAFS.

Figure 3 shows the obtained lattice parameters of the  $R-3m$  structure by LeBail and Rietveld refinements from the high-pressure SC-XRD experiment. As shown in Fig. 3(a), the values of  $a$  axis and  $c$  axis agree well between LeBail and Rietveld refinements over the entire pressure range. The  $c/a$

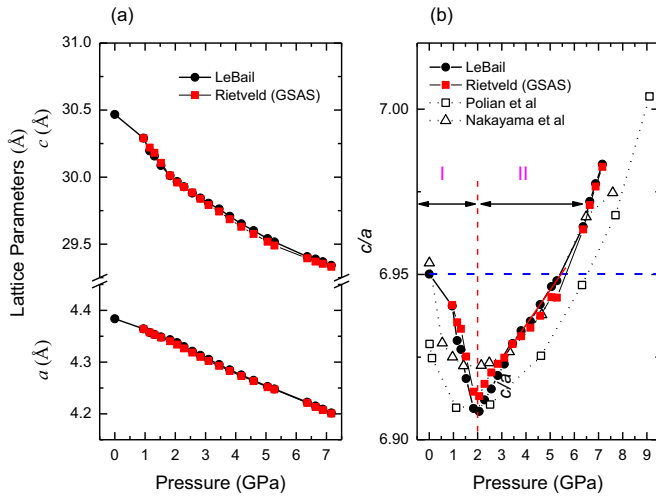


FIG. 3. (a) Lattice parameters of the  $R-3m$  phase of  $\text{Bi}_2\text{Te}_3$  at high pressure by LeBail refinement (black symbols) and GSAS Rietveld refinement (red symbols), respectively. (b) The corresponding  $c/a$  ratio together with the published data [22,24] for comparison. The vertical dashed line denotes the boundary between I ( $c$ -axis dominant compression) and II ( $a$ -axis dominant compression) of  $R-3m$  phase. Linear fit (red) highlights the steadiest range of the  $c/a$  ratio at 3.2–5.4 GPa.

ratio of  $R-3m$  phase [Fig. 3(b)] is consistent with previous data of powder x-ray diffraction [22,24]. The dashed horizontal line in the plot of  $c/a$  ratio [Fig. 3(b)] denotes a uniform compression of the  $R-3m$  unit cell at ambient pressure. The pressure dependences of the  $c/a$  ratio for both LeBail and Rietveld refinements show a profound sharp minimum at 2 GPa in comparison with previous data by powder x-ray diffraction [22,24]. This sharp minimum signifies a switching of the compression mechanism in  $\text{Bi}_2\text{Te}_3$  at high pressure. Below 2 GPa, the reduction of  $c$  axis is dominant over the  $a$  axis. Above 2 GPa, it switches to  $a$ -axis dominant compression gradually and further across the uniformly compressed line at 5.4 GPa. Thus, the  $R-3m$  phase can be divided into two distinct ranges, i.e., region I ( $c$ -axis dominant compression) and region II ( $a$ -axis dominant compression) [Fig. 3(b)]. This reversal in compression reflects the prominent role of van der Waals Te2-Te2 bonds along the  $c$  axis and is directly related to the ETT transition in  $\text{Bi}_2\text{Te}_3$ . The linear fitting line highlights the steadiest region of the  $c/a$  ratio by LeBail refinement at 3.2–5.4 GPa. The results (Fig. 3) support the viewpoint that SC-XRD under quasihydrostatic conditions provides superior accuracy on the lattice parameters than conventional powder x-ray diffraction at high pressure [18,39].

Figure 4 shows the selected XAFS data of  $\text{Bi}_2\text{Te}_3$  at Bi  $L_3$  edge as a function of pressure. Both the X-ray Absorption Near Edge Structure (XANES) and Extended X-ray Absorption Fine Structure (EXAFS) regions are free of DAC imposed glitches [Fig. 4(a)]. The corresponding  $k^2$ -weighted XAFS spectra,  $k^2\chi(k)$ , are of high quality with good signal/noise (S/N) ratio out to  $13 \text{ \AA}^{-1}$  [Fig. 4(b)]. This confirms that the DAC with NPD anvils is well suited to acquire high-quality XAFS data at high pressure [19,26,40] in contrast to the single-crystalline anvils where the residual glitches may spoil

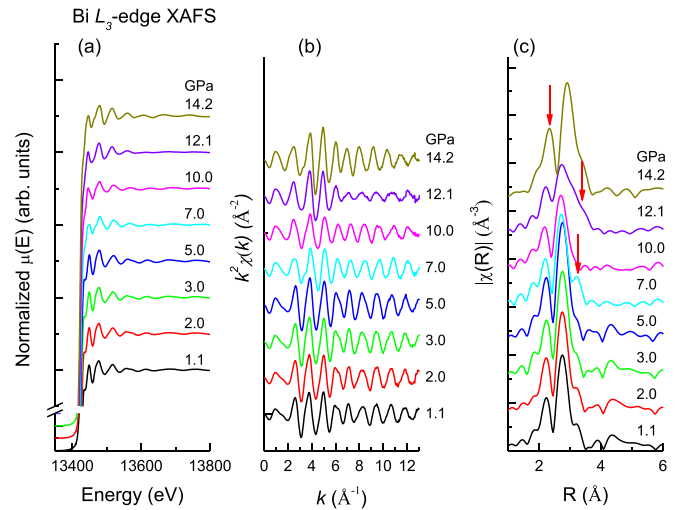


FIG. 4. Representative Bi  $L_3$ -edge XAFS spectra of  $\text{Bi}_2\text{Te}_3$  as a function of pressure using NPD anvils. (a) Normalized x-ray absorption  $\mu(E)$  free of DAC-imposed glitches. (b) Corresponding  $k^2$ -weighted XAFS spectra,  $k^2\chi(k)$ . (c) XAFS Fourier transform,  $|\chi(R)|$ , obtained in the range from 2.5 to  $12.4 \text{ \AA}^{-1}$  with a Hanning window. Note the significant changes (red arrows) at 7, 12, and 14 GPa as pressure increases.

the XAFS spectra and result in considerable uncertainties in the structural modeling [25].

As shown in Fig. 4(b), there is little change in the XAFS oscillation observed up to 5 GPa, but decreasing XAFS amplitude is noticeable in the pressure range of 7–12 GPa. The other increase in the amplitude of the XAFS oscillation is observed when the pressure is higher than 12 GPa. The atomic distribution in real space (no phase correction),  $|\chi(R)|$ , was obtained by Fourier transform of  $k^2\chi(k)$  in the range from 3 to  $12.4 \text{ \AA}^{-1}$  with a Hanning window of  $1.0 \text{ \AA}^{-1}$  width [Fig. 4(c)]. There is a remarkable change (red arrow) at 7 GPa where  $\text{Bi}_2\text{Te}_3$  remains largely in  $R-3m$  ( $\alpha\text{-Bi}_2\text{Te}_3$ ) phase (Figs. 1 and 3). A complete structural phase transition with narrow distributed local structure is completed at 10 GPa, which corresponds to the phase transition from  $R-3m$  structure to the monoclinic sevenfold  $C2/m$  structure ( $\beta\text{-Bi}_2\text{Te}_3$ ) [37]. A big shoulder (red arrow) appears at 12 GPa, but merges with the main peak at higher pressures, being a sign of another structural phase transition from  $C2/m$  to a monoclinic  $C2/c$  structure ( $\gamma\text{-Bi}_2\text{Te}_3$ ) [37]. At 14.2 GPa, a new shoulder peak (red arrow) emerges at lower distance, which indicates the appearance of the  $Im-3m$  phase ( $\delta\text{-Bi}_2\text{Te}_3$ ) that coexists with the  $C2/m$  ( $\beta\text{-Bi}_2\text{Te}_3$ ) and  $C2/c$  phases ( $\gamma\text{-Bi}_2\text{Te}_3$ ) [37,38]. These observations confirm that HP-XAFS is a good probe for the high-pressure phase transitions although it has remained largely unexploited so far.

Figure 5(a) shows the well-established first-shell fitting to the Bi  $L_3$ -edge XAFS data,  $|\chi(R)|$ , of  $\text{Bi}_2\text{Te}_3$  at 1.5 GPa. The inset shows the quintuple layer (QL) of five atomic planes with Te2-Bi-Te1-Bi-Te2 stacking along the  $c$  axis. Two FEFF (self-consistent real space multiple-scattering code) single paths of Bi-Te1 (central QL bond) and Bi-Te2 (outmost QL bond) in  $R-3m$  structure were used to fit the data in the range of 2.05 to  $3.5 \text{ \AA}^{-1}$  (no phase correction). The fitting

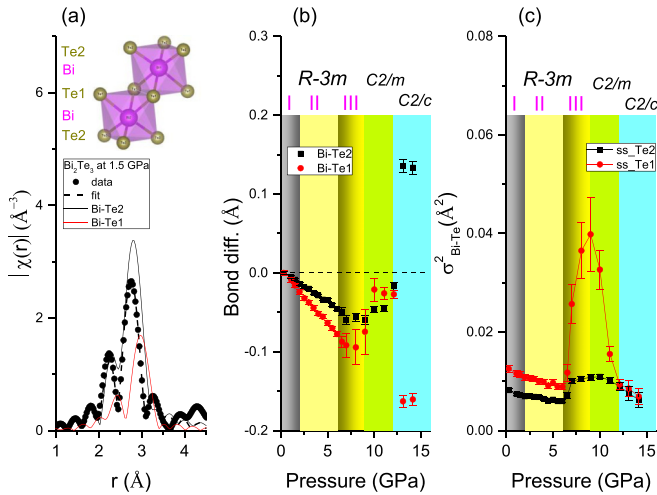


FIG. 5. (a) First-shell modeling of Bi  $L3$ -edge XAFS data,  $|\chi(r)|$ , at 1.5 GPa, as an example. The quintuple layer contains five atomic planes with Te2-Bi-Te1-Bi-Te2 stacking along the  $c$  axis. (b) Pressure dependence of the Bi-Te1 and Bi-Te2 bonds of  $\text{Bi}_2\text{Te}_3$  QL with respect to the values at the lowest pressure (0.29 GPa). (c) Pressure dependence of DW factor,  $\sigma^2$ . The  $R-3m$  phase can be divided into region I (0–2 GPa), region II (2–6 GPa), and region III (6–9 GPa).

at 1.5 GPa, as an example, shows a decent goodness-of-fit parameter,  $R_w$ , of 1.4%. To maintain the integrity of the first shell of  $R-3m$  structure, we made no change in the path degeneracies and relative amplitudes, but fitted the variables of bond distance and Debye-Waller (DW) factor,  $\sigma^2$ . The pressure dependences of bond deviations of  $r_{\text{Bi-Te1}}$  and  $r_{\text{Bi-Te2}}$  from the lowest pressure (0.29 GPa) are shown in Fig. 5(b), while the values of DW factor,  $\sigma^2$ , are plotted in Fig. 5(c).

The observed phase transitions at 7 GPa ( $R-3m$ ), 10 GPa ( $C2/m$ ), and 12 GPa ( $C2/c$ ) [Figs. 5(b) and 5(c)] agree well with previous XAFS studies [21]. Both the Bi-Te bond lengths [Fig. 5(b)] and DW factors [Fig. 5(c)] clearly shows that the region II of  $R-3m$  phase [Fig. 3(b)] can be further divided into region II (2–6 GPa) and region III (6–9 GPa). As shown in Fig. 5(c), It is worth noting that the DW factor exhibits an unusual pressure-induced ordering in the QLs in the  $R-3m$  phase up to 7 GPa. The ordering region spreads over regions I and II of  $R-3m$  phase [Fig. 5(c)]. This pressure-induced ordering inside QLs rules out the speculation that disorder may play a dominant role in the ETT or IPT transition [41], similar to the case of  $\text{Bi}_2\text{Se}_3$  [19]. Since the superconductivity (SC) emerges in region II at pressures above 3 GPa [9,10], disorder should not play a central role in the SC transition mechanism in the  $R-3m$  phase of  $\text{Bi}_2\text{Te}_3$ . Disorder effects on superconductivity were emphasized for some cuprates [42,43], but a comprehensive understanding of the interaction between superconductivity and disorder is still lacking [6].

Dramatic change in DW factors occurs at higher pressures. Before the phase transition from  $C2/m$  to  $C2/c$  structure at 12 GPa, there are two more distinguishable regions. In region III (6–9 GPa), the intralayer Bi-Te1 coordination of QLs undergoes an order-to-disorder transition with elongation of the Bi-Te1 bond length [Fig. 5(b)]. In the  $C2/m$  phase (9–12 GPa), the Bi-Te1 coordination undertakes an opposite

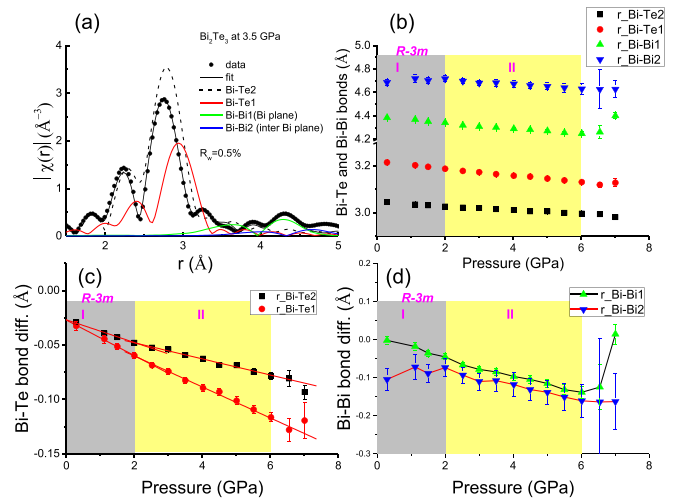


FIG. 6. (a) Representative structural modeling of Bi  $L3$ -edge XAFS data,  $|\chi(r)|$ , at 3.5 GPa within 4.7 Å; (b) Pressure dependence of  $\text{Bi}_2\text{Te}_3$  QL bonds: Bi-Te2, Bi-Te1, Bi-Bi1 (in Bi plane), and Bi-Bi2 (inter-Bi plane) bonds; (c) and (d) Deviations of the Bi-Te and Bi-Bi bonds from the ambient structure, respectively.

disorder-to-order transition. In both the  $R-3m$  region III and  $C2/m$  phase, the outmost Bi-Te2 coordination shows much smaller changes in the bond length and DW factor in contrast to the intra-QL Bi-Te1 bond. This order-disorder/disorder-order transition excludes the mechanism of a pressure-induced simple mixture of  $R-3m$  and  $C2/m$  phases from 7–12 GPa. In this pressure range, there should be a significant reconstruction in the QLs before the structural phase transition above 12 GPa ( $C2/c$  phase) [37].

The slight kink in the Bi-Te2 distances observed at 2 GPa [Fig. 5(b)] was firstly reported by previous XAFS studies [20] using conventional DACs, but it was not reproduced in a later XAFS measurement [21]. Furthermore, it was proposed that the distant Bi-Bi distance at 4.3 Å should associate with the ETT transition at  $\sim 5$  GPa [21]. This discrepancy between the high-pressure XAFS measurements may come from the residual small glitches [25] and the relatively narrow spectral range ( $< 11 \text{ \AA}^{-1}$ ) with conventional DACs [20,21], making it elusive how the closest Bi-Te distance under pressure changes during ETT in the  $R-3m$  phase of  $\text{Bi}_2\text{Te}_3$ .

It is known that both the pressure-induced ETT and topological superconductivity of  $\text{Bi}_2\text{Te}_3$  occur in the pure  $R-3m$  phase [10,13–15] of regions I and II. To unravel the mystery of the  $R-3m$  phase, it is necessary to make use of the XAFS data at large distances. Figure 6(a) shows a typical fit to the Bi  $L3$ -edge XAFS data of  $\text{Bi}_2\text{Te}_3$  at 3.5 GPa (full circles) using the full set of single scattering paths in the cluster of the  $R-3m$  structure within 4.7 Å. The fit is successful with a goodness-of-fit parameter,  $R_w$ , of 0.5% [Fig. 6(a)]. This modeling in the medium-range order provides more details about the QL local structure of  $\text{Bi}_2\text{Te}_3$  at high pressure: the ionic-covalent bonds of Bi-Te2, Bi-Te1, Bi-Bi1 (intra-Bi plane), and Bi-Bi2 (inter-Bi plane). To maintain the integrity of the  $R-3m$  cluster, no change in the path degeneracies and relative amplitudes, we used four variables of the bond distances of  $\text{Bi}_2\text{Te}_3$  QL to fit the data, as shown in Fig. 6(b).

TABLE I. Parameters of linear fit,  $y = a + bx$ , on the QL bonds of Bi-Te1 and Bi-Te2.

Bond	Bond type	Linear fit range (0–2 GPa)		Linear fit range (2–6.5 GPa)	
		$a$ (Å)	$b$ (Å/GPa)	$a$ (Å)	$b$ (Å/GPa)
Bi-Te1	Ionic-covalent	3.219 50(75)	−0.015 92(54)	3.215 61(173)	−0.014 28(38)
Bi-Te2	Ionic-covalent	3.047 63(75)	−0.010 98(55)	3.040 86(109)	−0.007 41(24)

Figures 6(c) and 6(d) show the pressure-induced deviation of the Bi-Te and Bi-Bi distances from the reported ambient  $R-3m$  structure [36], respectively. The intralayer ionic-covalent Bi-Te2 bond inside QL presents a change in the linear slope of pressure dependence at 2 GPa, which agrees with the pronounced dip of the  $c/a$  ratio [Fig. 3(b)]. The linear fitting parameters are listed in Table I. There is a pressure-induced synergistic change in the ionic-covalent–Te bonds during ETT. As shown in Table I, although the Bi-Te2 bond has a smaller pressure dependence than the central Bi-Te1 bond, its linear slope changes more obviously, i.e., twice the slope change of Bi-Te1 bond, at around 2 GPa [Fig. 6(c)]. Thus, the boundary of regions I and II in  $R-3m$  phase can be set at 2 GPa based on the SC-XRD (Fig. 3) and XAFS experiments [Fig. 6(c)]. From the pressure dependence of the Bi-Te bond length and the DW factor (Fig. 5), it can be roughly estimated that the boundary between regions II and III is 6 GPa. The interplane Bi-Bi2 bonds [blue down triangle, Fig. 6(d)] keep nearly constant upon the ETT transition.

These results indicate that changes of the intralayer Bi-Te1/Te2 bonds [Fig. 6(c)] and the Bi-Bi1 bond in Bi plane [Fig. 6(d)] should also be the driving forces of ETT in  $\text{Bi}_2\text{Te}_3$  in addition to the interlayer van der Waals Te2-Te2 bonds. The dramatic change in the  $c/a$  ratio [Fig. 3(b)] is associated with the ratio of interlayer/intralayer distance. A comparison between the local structure of Bi atoms (Fig. 6) and the lattice parameters (Fig. 3) would provide a comprehensive insight into the van der Waals Te2-Te2 bond upon compression. The length of  $c$  axis consists of the interplane Bi-Bi2 distance, ionic-covalent Bi-Te2 bond, and the van der Waals Te2-Te2 distances. Both the Bi-Te2 and interplane Bi-Bi2 distances show little change below 2 GPa [Figs. 6(c) and 6(d)]. Therefore, the large compression of the  $c$  axis [Fig. 3(a)] should be mainly attributed to the contribution of interlayer van der Waals Te2-Te2 bond between QLs. This is consistent with many previous high-pressure experiments of XRD, Raman, resistivity, and thermopower which have emphasized the roles of the outmost Te atoms and the interlayer van der Waals forces in the ETT in the layered TIs [7]. We can conclude that the van der Waals Te2-Te2 bond together with the ionic-covalent Bi-Te1, Bi-Te2, and Bi-Bi1 bonds drive the ETT, similar to the case of  $\text{Bi}_2\text{Se}_3$  [19], where the van der Waals Se2-Se2 bond can be directly measured by Se  $K$ -edge XAFS [19].

In addition, the value of the Bi-Te2 and Bi-Te1 bond lengths can also be derived from the  $R-3m$  structure of Rietveld refinement to cross check with the results of XAFS experiments. Figure 7 shows the comparison of the Bi-Te2 and the Bi-Te1 bond lengths between the XAFS experiment (black symbols) and an independent SC-XRD experiment. Although the overall pressure dependences of Rietveld refinement are

roughly consistent with those of XAFS, there exist considerable deviations in the Bi-Te2 and the Bi-Te1 bond lengths. The data obtained with (1 1 0) preferred orientation (red symbols) are slightly better than those of spherical harmonics in the preferred orientation model (blue symbols). Furthermore, the values of Bi-Te1 bond via Rietveld refinement with (1 1 0) preferred orientation show better agreement with XAFS data than that of Bi-Te2 bond. All the Bi-Te2/Te1 data of Rietveld refinements are quite scattered (Fig. 7). This discrepancy in the local structure highlights the value of XAFS as an important complementary tool for x-ray diffraction at high pressure (Fig. 3). Large uncertainties in the first-principles theoretical calculation on the electronic states of  $\text{Bi}_2\text{Te}_3$  would be inherited from the divergent local structure of Rietveld refinements (blue and red symbols, Fig. 7).

It is believed that the ETT is induced by a topological change of the Fermi surface if the Brillouin zone is strongly deformed, which is, however, difficult to probe experimentally [44]. To explore the electronic states of topological insulator  $\text{Bi}_2\text{Te}_3$  at high pressure, it is necessary to combine the experimental results of XAFS and SC-XRD into the first-principles theoretical calculation. We calculated the precise Wyckoff positions of Te atoms in the  $R-3m$  structure using the obtained values of Bi-Te2 and Bi-Te1 bonds [Fig. 6(b)] in combination with the lattice parameters of SC-XRD experiments (Fig. 3). We were then able to construct experimental structural models (crystallographic information files) up to 7 GPa for further first-principles calculations.

Figures 8(a) and 8(b) show the positions of the Bi (6c) and Te2 (6c) sites of  $R-3m$  structure by XAFS optimization

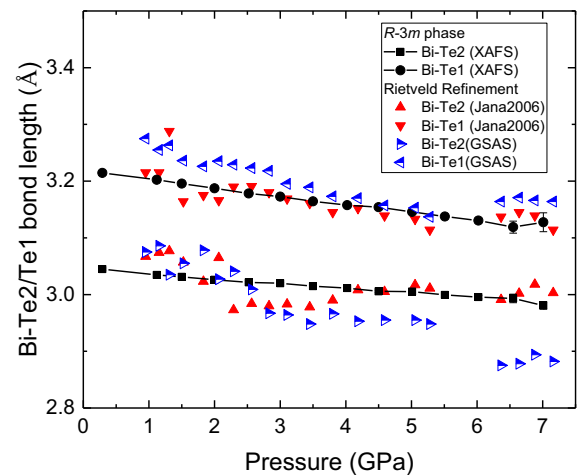


FIG. 7. Pressure dependence of Bi-Te2 and the Bi-Te1 bond lengths obtained by XAFS experiment (black symbols) in comparison with the results of Rietveld refinements of SC-XRD experiment using GSAS (blue symbols) and JANA2006 (red symbols).

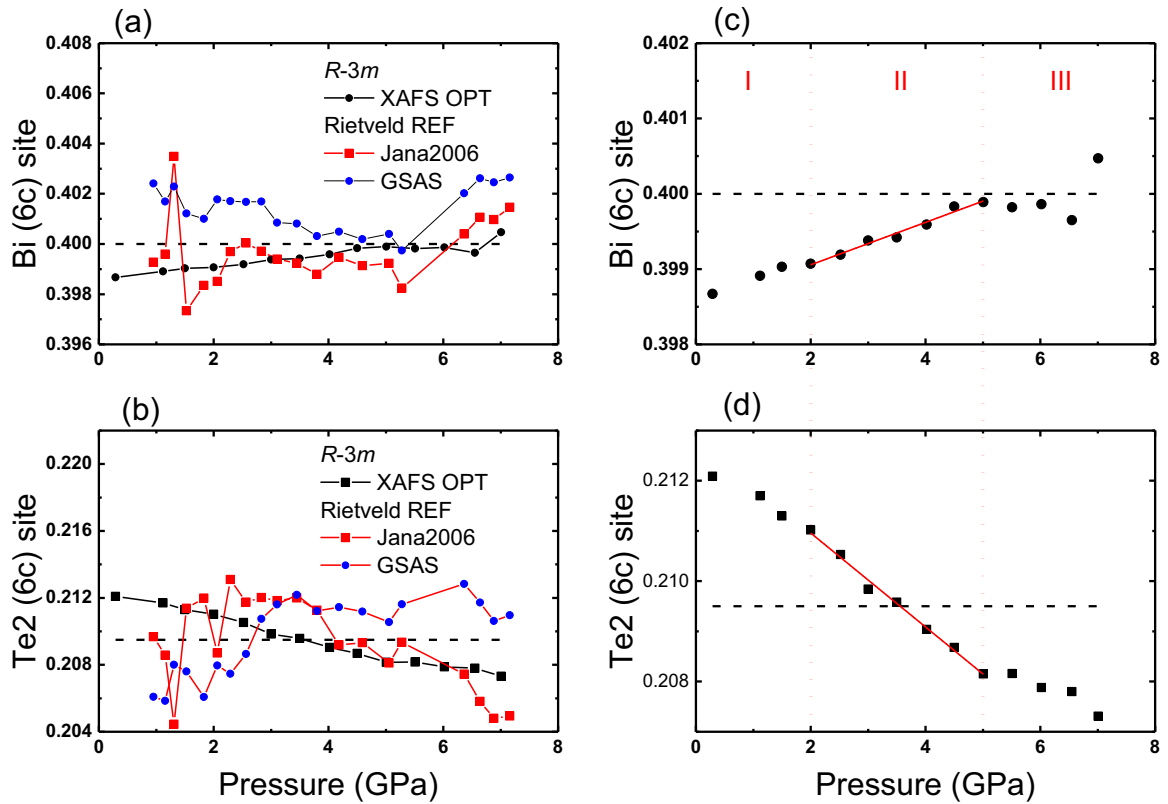


FIG. 8. Left panel: High-pressure behavior of (a) Bi (6c) site and (b) Te2 (6c) site of  $R-3m$  phase from the XAFS/SCXRD optimized structure (black symbols) in comparison with the structural parameters of Rietveld refinements by JANA2006 (red symbols) and GSAS (blue symbols). Right panel: The expanded plots of the XAFS/SCXRD optimized Bi (6c) site (c) and Te2 (6c) site (d) in  $R-3m$  structure, respectively. Red lines are the linear fits in the pressure range of 2–5 GPa to highlight the rapid changing range.

and Rietveld refinement of SC-XRD experiment, respectively. Values of the Bi (6c) and Te2 (6c) sites by Rietveld refinement are quite scattered, while the XAFS optimized structure shows good consistent pressure dependence. The preferred orientation of  $\text{Bi}_2\text{Te}_3$  crystal, which is employed in Rietveld refinement, has considerable influence on the positions of the Bi (6c) and Te2 (6c) sites in  $R-3m$  structure. The (1 1 0) preferred orientation (red symbols) shows a slightly better agreement with XAFS data than that of spherical harmonics model in the preferred orientation (blue symbols), as the case of Bi-Te2 and the Bi-Te1 bond lengths (Fig. 7). However, except the  $c/a$  ratio (Fig. 3), which provides good insight into the van der Waals forces during ETT, it is difficult to draw any solid conclusion about the ionic-covalent bond inside the QL of  $\text{Bi}_2\text{Te}_3$  based on the structural refinements (Figs. 7 and 8).

As shown in Figs. 8(c) and 8(d), it is clear that both the Bi (6c) and Te2 (6c) sites display relatively rapid changing but opposite pressure dependences. The linear fit at 2–5 GPa (red lines) yields linear equations of  $y = 0.3985 + 2.82 \times 10^{-4}x$  and  $y = 0.2128 - 9.36 \times 10^{-4}x$  for the Bi (6c) and Te2 (6c) sites, respectively, where  $x$  is the pressure and  $y$  is the position of Wyckoff site in the unit cell. The linear slope of Te2 (6c) position is more than three times the linear slope of Bi (6c) position, suggesting a prominent contribution of the outermost Te2 atoms in the surface of QLs [inset, Fig. 5(a)]. Above 5 GPa, there is almost no change in the position of Bi(6c) and Te2(6c) sites, indicating the existence of an intermediate state in the isostructural  $R-3m$  phase. Because the optimized struc-

tural parameters [Figs. 8(c) and 8(d)] are based on the XAFS and SC-XRD experiments, we can set the pressure boundary between regions II and III to 5 GPa, which is slightly smaller than the pressure boundary using the XAFS experiment alone (Fig. 5).

So far, it is believed that the ETT is an isostructural phase transition without modified Wyckoff positions of atoms and discontinuity in volume, but a pronounced change in the  $c/a$  ratio [Fig. 3(b)]. Our results show a different scenario for the pressure-induced changes in the  $c/a$  ratio and Wyckoff positions. The conflicting XRD proof for ETT in the topological insulators [7,14,22,24] may be owing to the difficulties in determining the precise Wyckoff positions of atoms in the crystal by conventional high-pressure powder XRD experiments, similar to the case of SC-XRD [Figs. 8(a) and 8(b)]. Figure 8 illustrates the importance of the local structure for the accurate structural models of  $\text{Bi}_2\text{Te}_3$  crystal since the accurate crystal structure is regarded as the key to understand the intriguing novel physics of TIs at high pressure. Recently, we demonstrated that local structure plays an important role for the electronic states of  $\text{Bi}_2\text{Se}_3$  [19].

Figure 9(a) shows the calculated band structure of  $\text{Bi}_2\text{Te}_3$  at high pressure including the spin-orbit coupling. The result at low pressure agrees with the published band structures of  $\text{Bi}_2\text{Te}_3$  [9,45]. From the expanded region at the  $\Gamma$  point [Fig. 9(b)], we find that the conduct band starts to indent at 2 GPa, and finally splits into two peaks above 3 GPa, i.e., the sign symbol reversed in the second-order derivative of

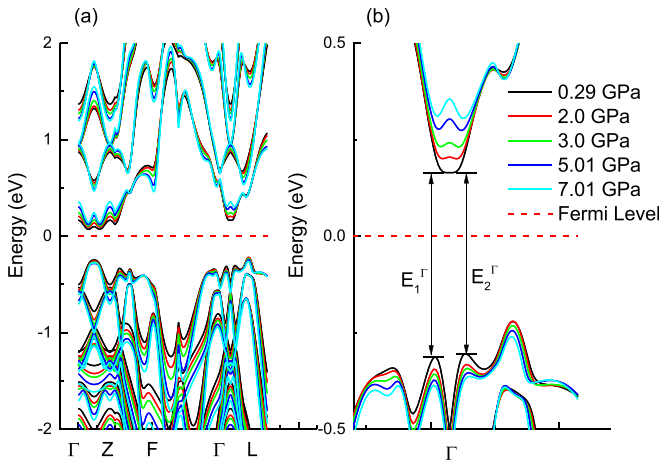


FIG. 9. (a) Calculated band structure of  $\text{Bi}_2\text{Te}_3$  including SOC. Notation for the high-symmetric points in the Brillouin zone is the same as in Ref. [2]; (b) Expanded region at  $\Gamma$  point. The valence band is slightly asymmetric at  $\Gamma$  point. The average direct band gap at  $\Gamma$  point is calculated by  $E_\Gamma = (E_1^\Gamma + E_2^\Gamma)$ .

conduct bands. This is a case of the ETT or Lifshitz transition [44] with changes in the conduct band extremum (Van Hove singularity). This result agrees well with previous studies [17]. Thus, we can conclude that the pressure-induced ETT in the  $R\text{-}3m$  phase of  $\text{Bi}_2\text{Te}_3$  is completed at 2 GPa.

There are also two interesting pressure-induced physical property changes in the isostructural  $R\text{-}3m$  phase of  $\text{Bi}_2\text{Te}_3$ , i.e., the metallization from ambient pressure to 3 GPa [15] and the emergence of superconductivity above 3 GPa [9,10]. The emergence of topological superconductivity is one of the most intriguing novel physics for the prototypical 3D topological insulators ( $\text{Bi}_2\text{Se}_3$ ,  $\text{Bi}_2\text{Te}_3$ , and  $\text{Sb}_2\text{Te}_3$ ) [7–10]. Interestingly, superconductivity was discovered in the  $R\text{-}3m$  phase of the topological insulator  $\text{Bi}_2\text{Te}_3$  [9,10] and  $\text{Sb}_2\text{Te}_3$  [46], but not for  $\text{Bi}_2\text{Se}_3$  somehow [47]. The ETT of  $\text{Bi}_2\text{Te}_3$  can be explained with the XAFS optimized structure (Fig. 9). However, the effect of pressure on the superconductivity is very complex in general [6]. Two intrinsic pressure variables, i.e., the carrier concentration and the pairing interaction strength, can be employed to explain the pressure effect on the superconductivity for cuprates [48,49]. These two inherent pressure variables are directly related to the energy gap. Therefore, an accurate theoretical calculation of the band gap is very important for understanding the pressure-induced superconductivity in  $\text{Bi}_2\text{Te}_3$ .

Figure 10 shows the calculated direct and indirect band gaps of the XAFS optimized  $R\text{-}3m$  structure of  $\text{Bi}_2\text{Te}_3$  as a function of pressure together with the values of previous studies of  $\text{Bi}_2\text{Se}_3$  by Segura *et al.* [17], Bera *et al.* [14], and Hong *et al.* [19] for comparison. Identification of the common features and differences of the band gap is necessary for a better understanding of the novel physics in 3D topological insulators. Detailed comparative experimental and theoretical studies may provide important clues about the origin of superconductivity, e.g., why  $\text{Bi}_2\text{Te}_3$  is a superconductor in the  $R\text{-}3m$  phase but  $\text{Bi}_2\text{Se}_3$  is not.

As shown in Fig. 10(a), all the direct band gaps of  $\text{Bi}_2\text{Te}_3$  and  $\text{Bi}_2\text{Se}_3$  at  $\Gamma$  point keep opening as pressure increases,

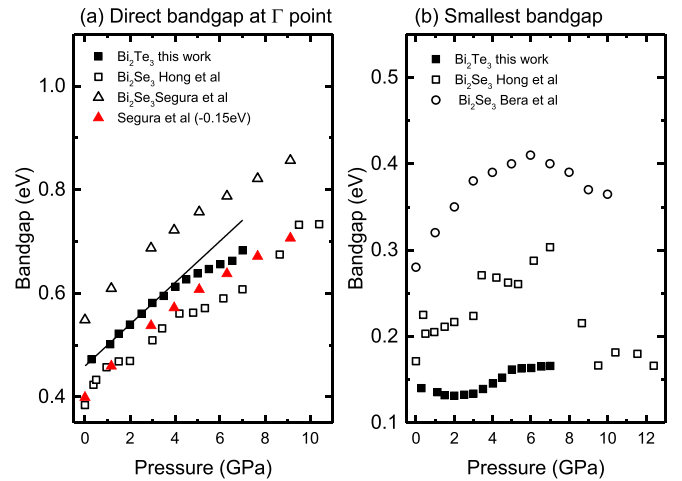


FIG. 10. Calculated band gap of  $\text{Bi}_2\text{Te}_3$  as a function of pressure: (a) direct band gap at  $\Gamma$  point and (b) the smallest band gap together with the values of previous studies of  $\text{Bi}_2\text{Se}_3$  by Hong *et al.* [19], Segura *et al.* [17], and Bera *et al.* [14] for comparison.

while the pressure dependence of  $\text{Bi}_2\text{Te}_3$  band gap shows fewer features than that of  $\text{Bi}_2\text{Se}_3$  at high pressure [19]. It maintains almost a linear behavior at pressure below 4 GPa, but gradually deviates from the linear relationship at pressures above 5 GPa. More detailed comparison of  $\text{Bi}_2\text{Te}_3$  with the published data can be found elsewhere [19]. For the indirect band gap [Fig. 10(b)], the value of  $\text{Bi}_2\text{Te}_3$  is smaller than that of  $\text{Bi}_2\text{Se}_3$ , which is consistent with experimental observation [17,50,51]. It is noteworthy that there is a similar region of plateau located at 5–7 GPa and 3–7 GPa for  $\text{Bi}_2\text{Te}_3$  and  $\text{Bi}_2\text{Se}_3$ , respectively. Further work on  $\text{Sb}_2\text{Te}_3$  is desired to clarify if such a plateau is a shared feature for the 3D topological insulators.

The metallization of  $\text{Bi}_2\text{Te}_3$  occurs at 0–3 GPa [15] [Fig. 10(b)], while it is 7–9.5 GPa for  $\text{Bi}_2\text{Se}_3$  [19,52]. Interestingly, both the pressure-induced metallization processes occur before the emergence of topological superconductivity of  $\text{Bi}_2\text{Te}_3$  at 3 GPa [9,10] and  $\text{Bi}_2\text{Se}_3$  at 11 GPa [47], respectively. This pressure-induced metallization would increase the carrier concentration, which serves as one of two intrinsic pressure variables for the explanation of superconductivity in cuprates [48,49]. It is also very intriguing that in the superconductivity regions of  $\text{Bi}_2\text{Te}_3$  (>3 GPa) and  $\text{Bi}_2\text{Se}_3$  (>11 GPa), the indirect band gaps show similar values of 0.14–0.18 eV. This band-gap value may be necessary for the enhancement of pairing interaction strength and eventually causing the emergence of superconductivity in  $\text{Bi}_2\text{Te}_3$  above 3 GPa [9,10] and  $\text{Bi}_2\text{Se}_3$  above 11 GPa [47]. As a result, these observed features of  $\text{Bi}_2\text{Te}_3$  and  $\text{Bi}_2\text{Se}_3$  band gaps may provide important clues about the origin of superconductivity and the possibility of topological superconductivity. Further theoretical studies based on the XAFS optimized structures would be very helpful for the elucidation of superconductivity in  $\text{Bi}_2\text{Se}_3$  and  $\text{Bi}_2\text{Te}_3$  topological insulators.

Figure 11 shows the calculated indirect band gap of  $\text{Bi}_2\text{Te}_3$  at high pressure together with the previously reported experimental data. The vertical dashed lines mark the three



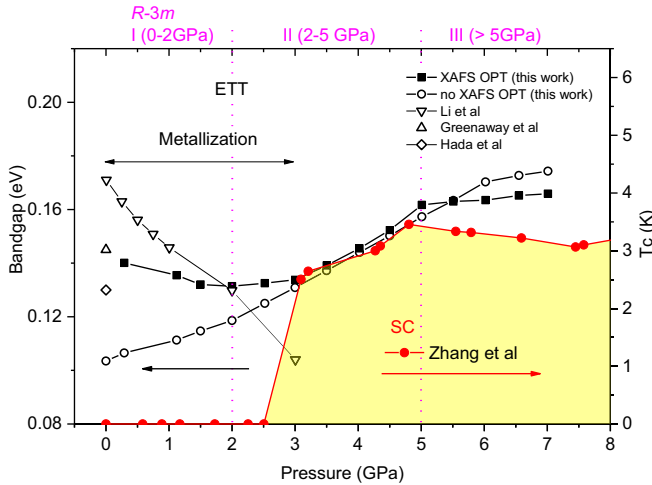


FIG. 11. The calculated band gap of  $\text{Bi}_2\text{Te}_3$   $R\text{-}3m$  phase including SOC. Values of unoptimized structure and experimental data of infrared spectroscopy [50], optical experiments [51], and resistivity measurements [15] are shown for comparison. Right axis shows the superconducting transition temperature of the  $R\text{-}3m$  phase from Ref. [10]. Vertical lines mark the boundaries of the three regions in the  $R\text{-}3m$  phase of  $\text{Bi}_2\text{Te}_3$ .

regions of the  $R\text{-}3m$  phase defined by the SC-XRD and HP-XAFS experiments (Figs. 3, 5, and 8). The indirect band gap of the XAFS optimized structure at 0.29 GPa is 0.14 eV, which agrees well with the values of 0.13 eV by infrared spectroscopy [50], 0.145 eV by optical reflectivity/absorption experiments [51], and 0.171 eV by resistivity measurements [15] at ambient pressure. As pressure increases, the band gap of XAFS optimized structure decreases noticeably, forming a minimum at 2 GPa (Fig. 11). For XAFS optimized structures, this reduction and further increase in band gap seems to be an unusual behavior, but it is consistent with the experimental observations. The pressure-induced metallization of  $\text{Bi}_2\text{Te}_3$  was reported with energy band gap changing from 0.171 eV ambient pressure to 0.104 eV at 3 GPa [15] (down triangle, Fig. 11). Moreover, the pressure-induced initial band-gap narrowing should give rise to the increase of carrier concentration, i.e., decrease in the Hall coefficient  $R_H$ , which was indeed observed previously [10]. This band-gap narrowing complies with the common pressure effects that applying pressure generally increases the concentration of the charge carriers as in the case of cuprates [6]. It is worth noting that there is considerable difference in the indirect band gap between the XAFS optimized and unoptimized  $R\text{-}3m$  structures. The indirect band gap of the unoptimized  $R\text{-}3m$  structure shows less correlation with the ETT and metallization, as it just keeps opening as pressure increases. These results indicate that the local structure plays an important role in the proper interpretation of ETT and the metallization of  $\text{Bi}_2\text{Te}_3$  at high pressure. However, at pressures above 3 GPa, the band-gap value of the unoptimized structure is quite consistent with the value of the XAFS optimized structure. Thus, the pressure-induced change of lattice parameters (Fig. 3) should become a leading role for the overall band-gap opening at pressures above 3 GPa.

The indirect band gap of the XAFS optimized  $R\text{-}3m$  structure opens at 3–5 GPa, but surprisingly remains nearly constant at pressures above 5 GPa, which is consistent with the observed intermediate state [region III of  $R\text{-}3m$ , Figs. 8(c) and 8(d)]. For comparison, Fig. 11 also shows the superconducting transition temperature ( $T_c$ ) of the  $\text{Bi}_2\text{Te}_3$  single crystal in the  $R\text{-}3m$  phase (red points) that is taken from Ref. [10]. The superconductivity of  $\text{Bi}_2\text{Te}_3$  emerges and enhances in region II (2–5 GPa), but changes little in region III (above 5 GPa). There is a striking correlation between the indirect band gap of the XAFS optimized structure and the superconductivity of  $\text{Bi}_2\text{Te}_3$  in the II and III regions of the  $R\text{-}3m$  phase. It is known that, for the pressure effect of the most optimally doped compounds,  $T_c$  initially increases in general, reaches a saturation point (critical pressure), and then decreases gradually [6]. The inflection point of the indirect band gap at the boundary between regions II and III, i.e., the second IPT of the  $R\text{-}3m$  phase, is very consistent with the  $T_c$  critical saturation pressure of  $\text{Bi}_2\text{Te}_3$  single crystal. This provides clues that the superconductivity of  $\text{Bi}_2\text{Te}_3$  should be attributed to the structural change of bulk  $R\text{-}3m$  phase, supporting the speculation that the bulk state of  $\text{Bi}_2\text{Te}_3$  could be a topological superconductor [9]. It has been reported that the topological superconductivity of  $\text{Bi}_2\text{Te}_3$  can be realized due to the proximity effect between Dirac-type surface states and the superconducting bulk states [9]. Further work on the interplay between the bulk states and Dirac-type surface states using the XAFS optimized crystalline structures is required. The present study provides the structural origin for the novel physics in the bulk  $R\text{-}3m$  phase of topological insulator  $\text{Bi}_2\text{Te}_3$  at high pressure.

#### IV. CONCLUSION

In summary, we report a combined investigation of SC-XRD, HP-XAFS, and first-principle calculations, which were able to probe the subtle changes in the local structure and isostructural electronic state in the  $R\text{-}3m$  phase of the topological insulator  $\text{Bi}_2\text{Te}_3$  at high pressure. The study reveals that the characteristic structural variations are consistent with physical properties including the isostructural phase transition (IPT or ETT), metallization, and topological superconductivity. Our results demonstrate that the local structure plays a critical role in the electronic states of the topological insulator  $\text{Bi}_2\text{Te}_3$  under high pressure.

#### ACKNOWLEDGMENTS

We would like to thank T. Lanzirrotti, S. Tkachev, X.M. Yu, and N. Lazarz for their assistance with the experiments. Comments from Freyja O'Toole and two anonymous reviewers improved the manuscript. HPSTAR is supported by the National Natural Science Foundation of China (Grants No. U1530402 and No. U1930401). The GSECARS sector of APS is supported by NSF (Grant No. EAR-1634415) and DOE (Grant No. DE-FG02-94ER14466). H.K.M. was supported by NSF Grants No. EAR-1345112 and No. EAR-1447438. Y.D. acknowledges the support from National Key Research and Development Program of China (Grant No. 2018YFA0305703), Science Challenge Project (Project No.

TZ2016001), and The National Natural Science Foundation of China (Grants No. U1930401 and No. 11874075). The data

that support the findings of this study are available from the corresponding author upon reasonable request.

- 
- [1] H. Zhang, C.-X. Liu, X.-L. Qi, X. Dai, Z. Fang, and S.-C. Zhang, *Nat. Phys.* **5**, 438 (2009).
- [2] X.-L. Qi and S.-C. Zhang, *Phys. Today* **63**, 1, 33 (2009).
- [3] Y. L. Chen, J. G. Analytis, J. H. Chu, Z. K. Liu, S. K. Mo, X. L. Qi, H. J. Zhang, D. H. Lu, X. Dai, Z. Fang *et al.*, *Science* **325**, 178 (2009).
- [4] D. Hsieh, Y. Xia, D. Qian, L. Wray, F. Meier, J. H. Dil, J. Osterwalder, L. Patthey, A. V. Fedorov, H. Lin *et al.*, *Phys. Rev. Lett.* **103**, 146401 (2009).
- [5] X.-L. Qi and S.-C. Zhang, *Rev. Mod. Phys.* **83**, 1057 (2011).
- [6] H.-K. Mao, X.-J. Chen, Y. Ding, B. Li, and L. Wang, *Rev. Mod. Phys.* **90**, 015007 (2018).
- [7] F. J. Manjón, R. Vilaplana, O. Gomis, E. Pérez-González, D. Santamaría-Pérez, V. Marín-Borrás, A. Segura, J. González, P. Rodríguez-Hernández, A. Muñoz *et al.*, *Phys. Status Solidi B* **250**, 669 (2013).
- [8] M. Einaga, Y. Tanabe, A. Nakayama, A. Ohmura, F. Ishikawa, and Y. Yamada, *J. Phys.: Conf. Ser.* **215**, 012036 (2010).
- [9] J. L. Zhang, S. J. Zhang, H. M. Weng, W. Zhang, L. X. Yang, Q. Q. Liu, S. M. Feng, X. C. Wang, R. C. Yu, L. Z. Cao *et al.*, *Proc. Natl. Acad. Sci. USA* **108**, 24 (2011).
- [10] C. Zhang, L. Sun, Z. Chen, X. Zhou, Q. Wu, W. Yi, J. Guo, X. Dong, and Z. Zhao, *Phys. Rev. B* **83**, 140504(R) (2011).
- [11] E. S. Itskovich, L. M. Kashirskaya, and V. F. Kraidenov, *Semiconductors* **31**, 276 (1997).
- [12] N. V. Chandra Shekar, D. A. Polvani, J. F. Meng, and J. V. Badding, *Phys. B: Condens. Matter* **358**, 14 (2005).
- [13] G. K. Pradhan, A. Bera, P. Kumar, D. V. S. Muthu, and A. K. Sood, *Solid State Commun.* **152**, 284 (2012).
- [14] A. Bera, P. Koushik, D. V. S. Muthu, U. V. Waghmare, and A. K. Sood, *J. Phys.: Condens. Matter* **28**, 105401 (2016).
- [15] C. Y. Li, A. L. Ruoff, and C. W. Spencer, *J. Appl. Phys.* **32**, 1733 (1961).
- [16] J.-I. Zhang, S.-J. Zhang, H.-M. Weng, W. Zhang, L.-X. Yang, Q.-Q. Liu, P.-P. Kong, J. Zhu, S.-M. Feng, X.-C. Wang *et al.*, *Front. Phys.* **7**, 193 (2012).
- [17] A. Segura, V. Panchal, J. F. Sánchez-Royo, V. Marín-Borrás, V. Muñoz-Sanjosé, P. Rodríguez-Hernández, A. Muñoz, E. Pérez-González, F. J. Manjón, and J. González, *Phys. Rev. B* **85**, 195139 (2012).
- [18] G. Shen and H. K. Mao, *Rep. Prog. Phys.* **80**, 016101 (2016).
- [19] X. Hong, M. Newville, Y. Ding, T. Irifune, G. Gu, and H.-K. Mao, *Phys. Rev. B* **101**, 214107 (2020).
- [20] H. Zhu, J. Dong, P. Li, Y. Wang, Z. Guo, X. Shan, Y. Gong, P. An, X. Li, J. Zhang *et al.*, *Phys. Status Solidi B* **254**, 1700007 (2017).
- [21] Z. Guo, H. Zhu, J. Dong, Q. Jia, Y. Gong, Y. Wang, H. Li, P. An, D. Yang, Y. Zhao *et al.*, *J. Appl. Phys.* **124**, 065901 (2018).
- [22] A. Nakayama, M. Einaga, Y. Tanabe, S. Nakano, F. Ishikawa, and Y. Yamada, *High Pressure Res.* **29**, 245 (2009).
- [23] R. Vilaplana, D. Santamaría-Pérez, O. Gomis, F. J. Manjón, J. González, A. Segura, A. Muñoz, P. Rodríguez-Hernández, E. Pérez-González, V. Marín-Borrás *et al.*, *Phys. Rev. B* **84**, 184110 (2011).
- [24] A. Polian, M. Gauthier, S. M. Souza, D. M. Trichês, J. Cardoso de Lima, and T. A. Grandi, *Phys. Rev. B* **83**, 113106 (2011).
- [25] X. Hong, M. Newville, V. B. Prakapenka, M. L. Rivers, and S. R. Sutton, *Rev. Sci. Instrum.* **80**, 073908 (2009).
- [26] N. Ishimatsu, K. Matsumoto, H. Maruyama, N. Kawamura, M. Mizumaki, H. Sumiya, and T. Irifune, *J. Synchrotron Radiat.* **19**, 768 (2012).
- [27] H. K. Mao, J. Xu, and P. M. Bell, *J. Geophys. Res.: Solid Earth* **91**, 4673 (1986).
- [28] A. P. Hammersley, S. O. Svensson, M. Hanfland, A. N. Fitch, and D. Hausermann, *High Pressure Res.* **14**, 235 (1996).
- [29] V. Peřířek, M. Dušek, and L. Palatinus, *Zeitschrift für Kristallographie - Crystalline Materials* **229**, 345 (2014).
- [30] B. Toby, *J. Appl. Crystallogr.* **34**, 210 (2001).
- [31] B. Ravel and M. Newville, *J. Synchrotron Radiat.* **12**, 537 (2005).
- [32] M. Newville, *J. Synchrotron Radiat.* **8**, 96 (2001).
- [33] J. P. Perdew and A. Zunger, *Phys. Rev. B* **23**, 5048 (1981).
- [34] X. Hua, X. Chen, and W. A. Goddard, *Phys. Rev. B* **55**, 16103 (1997).
- [35] P. Giannozzi, S. Baroni, N. Bonini, M. Calandra, R. Car, C. Cavazzoni, D. Ceresoli, G. L. Chiarotti, M. Cococcioni, I. Dabo *et al.*, *J. Phys.: Condens. Matter* **21**, 395502 (2009).
- [36] S. Nakajima, *J. Phys. Chem. Solids* **24**, 479 (1963).
- [37] L. Zhu, H. Wang, Y. Wang, J. Lv, Y. Ma, Q. Cui, Y. Ma, and G. Zou, *Phys. Rev. Lett.* **106**, 145501 (2011).
- [38] M. Einaga, A. Ohmura, A. Nakayama, F. Ishikawa, Y. Yamada, and S. Nakano, *Phys. Rev. B* **83**, 092102 (2011).
- [39] T. S. Duffy, *Rep. Prog. Phys.* **68**, 1811 (2005).
- [40] T. Irifune, A. Kurio, S. Sakamoto, T. Inoue, and H. Sumiya, *Nature (London)* **421**, 599 (2003).
- [41] B. Wölfing, C. Kloc, J. Teubner, and E. Bucher, *Phys. Rev. Lett.* **86**, 4350 (2001).
- [42] M. Calamiotou, A. Gantis, E. Siranidi, D. Lampakis, J. Karpinski, and E. Liarokapis, *Phys. Rev. B* **80**, 214517 (2009).
- [43] J.-B. Zhang, V. V. Struzhkin, W. Yang, H.-K. Mao, H.-Q. Lin, Y.-C. Ma, N.-L. Wang, and X.-J. Chen, *J. Phys.: Condens. Matter* **27**, 445701 (2015).
- [44] I. M. Lifshitz, *Sov. Phys. JETP (USSR)* **11**, 1130 (1960).
- [45] S. K. Mishra, S. Satpathy, and O. Jepsen, *J. Phys.: Condens. Matter* **9**, 461 (1997).
- [46] J. Zhu, J. L. Zhang, P. P. Kong, S. J. Zhang, X. H. Yu, J. L. Zhu, Q. Q. Liu, X. Li, R. C. Yu, R. Ahuja *et al.*, *Sci. Rep.* **3**, 2016 (2013).
- [47] K. Kirshenbaum, P. S. Syers, A. P. Hope, N. P. Butch, J. R. Jeffries, S. T. Weir, J. J. Hamlin, M. B. Maple, Y. K. Vohra, and J. Paglione, *Phys. Rev. Lett.* **111**, 087001 (2013).
- [48] X. J. Chen, H. Q. Lin, and C. D. Gong, *Phys. Rev. Lett.* **85**, 2180 (2000).

- [49] X.-J. Chen, V. V. Struzhkin, R. J. Hemley, H.-K. Mao, and C. Kendziora, *Phys. Rev. B* **70**, 214502 (2004).
- [50] M. Hada, K. Norimatsu, S. i. Tanaka, S. Keskin, T. Tsuruta, K. Igarashi, T. Ishikawa, Y. Kayanuma, R. J. D. Miller, K. Onda *et al.*, *J. Chem. Phys.* **145**, 024504 (2016).
- [51] D. L. Greenaway and G. Harbeke, *J. Phys. Chem. Solids* **26**, 1585 (1965).
- [52] J. Zhang, Y. Han, C. Liu, X. Zhang, F. Ke, G. Peng, Y. Ma, Y. Ma, and C. Gao, *Appl. Phys. Lett.* **105**, 062102 (2014).